Role of T_e/T_i and ∇v_{tor} in Ion Heat Transport of ASDEX Upgrade H-mode Plasmas

A. Manini[1], C. Angioni[1], A. G. Peeters[1], F. Ryter[1], A. Jacchia[2], C. F. Maggi[1], W. Suttrop[1] and the ASDEX Upgrade Team

[1]Max-Planck-Institut für Plasmaphysik, Association EURATOM-IPP, 85748 Garching, Germany
[2]Istituto di Fisica del Plasma, Association EURATOM-ENEA-CNR, 20125 Milano, Italy

February 12, 2007

Abstract

Experiments in H-mode plasmas have shown that both heat and particle transport are sensitive to the ratio between electron and ion temperature (T_e/T_i). While decreasing T_e/T_i is beneficial for confinement, an increased electron heating in these so called "hot ion plasmas" deteriorates the confinement. H-mode plasmas with low T_e/T_i are often accompanied by high toroidal rotation velocity (v_ϕ). Its gradient (∇v_ϕ) can destabilise the ion temperature gradient mode (ITG) through its parallel component in the parallel velocity shear, but it has also stabilising effects since it produces an $E \times B$ shearing rate ($\omega_{E\times B}$). In this paper, the effects of electron heating on the ion heat transport is investigated in H-mode plasmas heated by neutral beam injection (NBI) and electron cyclotron heating (ECH). In particular, the correlation on T_e/T_i and ∇v_ϕ is studied and compared with calculations made with GLF23 and GS2. Experimentally it is shown that the normalised gradient length of the ions (R/L_{T_i}) is correlated to both T_e/T_i and ∇v_ϕ: peaked ion temperature profiles are only obtained with low T_e/T_i and high ∇v_ϕ, and vice-versa. When ECH is added, both ion heat and momentum transport are enhanced, leading to a drop of both the T_i and v_ϕ profiles. The effective growth rate $\gamma_{eff} = \gamma - \omega_{E\times B}$ is calculated, with the mode growth rate γ determined with GS2 and $\omega_{E\times B}$ with GLF23. The ion transport is enhanced due to the decrease of the ITG R/L_{T_i} threshold with increasing T_e/T_i. Comparison of the dependence of R/L_{T_i} on T_e/T_i and ∇v_ϕ between experiments and modelling indicates that the deterioration of confinement cannot be explained by the changes in only T_e/T_i or ∇v_ϕ, but by the combined effects of both parameters. The changes in T_e/T_i act directly on the ITG threshold, while the ones in ∇v_ϕ modify the $\omega_{E\times B}$ shearing rate leading to changes in the effective threshold.

1 Introduction

The understanding of the energy transport in a fusion plasma is a very important issue because it directly determines the plasma performance, hence it is crucial for predicting future devices. Recently, significant progress has been made in the investigation of the electron heat transport in L-mode plasmas with pure electron heating added to ohmic plasmas [1, 2, 3, 4, 5, 6, 7, 8]. In contrast to these cases, in which the electron temperature is larger than the ion temperature ($T_e > T_i$), the transport in plasmas with dominant ion heating ($T_e \leq T_i$), and particularly in H-mode, has not been thoroughly understood yet. This range of operation is particularly important because a large number of previous studies has shown that the performance is significantly improved in plasmas with $T_i > T_e$. Examples are the hot ion H-modes in DIII-D [9] and JET [10], the "supershot" in TFTR [11] and the advanced scenarios in ASDEX Upgrade [12]. However, in future reactors, because of the dominant electron heating in the centre and of collisional coupling, a ratio $T_e/T_i \geq 1$ is expected. It is therefore important to understand the dependence of transport on T_e/T_i. Experimentally, this question has been addressed in ASDEX Upgrade [13, 14], DIII-D [16, 17] and JET [18, 19, 20]. In all these experiments it has been observed that the hot ion regime, whose transport properties

are governed by the ion temperature gradient (ITG) instability, deteriorates when electron heating increases. For the ITG, theory predicts that T_e/T_i is destabilising. In the modelling of the effects of T_e/T_i in JET hot ion and hot electron regimes [19, 20], the existence of feedback loops involving T_e/T_i and its relationship to the ITG threshold has been invoked to explain the deterioration of transport when either T_e is increased, or T_i is decreased. In addition, other studies have pointed out the strong link between ion heat and momentum transport [21, 22, 23]. Theory predicts [23] that the parallel velocity shear, $\nabla v_\parallel$, has a destabilising effect on the ITG. Consequently, the gradient of the toroidal velocity, ∇v_ϕ, might induce a destabilisation due to its parallel component. On the other hand, ∇v_ϕ has also a stabilising effect since it produces an $E \times B$ shearing rate, $\omega_{E\times B}$. The effect of rotation on H-mode transport has been studied, at constant T_e/T_i, in DIII-D [24], where it has been shown that the ion heat and particle transport are sensitive to the change in rotation direction and magnitude. It follows that we are in presence of a competition between two effects induced by ∇v_ϕ: one destabilising ($\nabla v_\parallel$) and the other stabilising ($\omega_{E\times B}$). The aim of the present paper is to experimentally analyse the dependence of the ion heat transport on both T_e/T_i and ∇v_ϕ and to compare the experimental observations with theory based models.

The paper is organised as follows: in section 2 we present the main experimental observations; in section 3 the modelling is performed and its results are compared with the experimental observations; summary and conclusions are drawn in section 4.

2 Experimental observations

A set of ASDEX Upgrade ELMy H-mode plasmas in deuterium is considered. The main parameters of these discharges are $I_p = 1.0MA$, $2.4 < |B_T| < 2.6$, $4 < q_{95} < 5$, $\kappa = 1.75$ and $\delta = 0.15$. All are heated with $5.0MW$ NBI. In addition, in some of them [14], electron cyclotron heating (ECH) is added at different power levels ($0.2MW < P_{ECH} < 2.0MW$) and at different radial locations ($0.1 < \rho_t < 0.6$, with ρ_t being the normalised toroidal flux radius). The electron temperature was measured by the electron cyclotron emission diagnostic, the ion temperature and the plasma toroidal velocity by the charge exchange recombination spectroscopy diagnostic using the carbon C^{6+} charge exchange line at $529.05nm$. The line averaged density is derived from the interferometer. The general behaviour of all these discharges is characterised by a progressive increase of T_e/T_i with increasing density. As usual, T_e and T_i decrease with increasing density, however T_i is more sensitive and T_e/T_i changes mostly accordingly to the T_i variations. Figure 1 shows the dependence of central ion (T_{i0}) and electron (T_{e0}) temperatures and of T_{e0}/T_{i0} with respect to the line averaged electron density $\overline{n}_e$. The points shown in the figure are from phases with NBI only. The strongest variations occur at the lowest densities, typically for $\overline{n}_e < 6.0 \cdot 10^{19} m^{-3}$. At these densities, low collisional coupling between electrons and ions is obtained. For $\overline{n}_e < 5.0 \cdot 10^{19} m^{-3}$ in particular, the power delivered to the ions is approximately $60-70\%$ of the injected NBI power and only $20-25\%$ is delivered to the electrons, while $10-15\%$ are power losses shared between orbit losses and charge exchange recombination at the edge [14]. This explains the stronger increase of T_{i0} compared to T_{e0}. As a consequence, the temperature ratio T_{e0}/T_{i0} changes from values around unity for the higher densities, to values significantly below 1 for the lower densities.

We now focus on a subset of discharges with $\overline{n}_e < 6.0 \cdot 10^{19} m^{-3}$ that include a series of experiments for which the electron heat transport has been studied and reported in [14], and we analyse the ion heat transport. In addition to the $5.0MW$ NBI-only phase, several of these discharges also present phases in which up to $2.0MW$ of ECH were added. Figure 2 shows the behaviour of T_e and T_i at $\rho_t = 0.5$ with respect to $\overline{n}_e$. Consistently with the previous figures, also at this radial position both T_e and T_i increase with decreasing density. With only NBI, the increase of T_i is stronger than that of T_e, leading to low values of T_e/T_i. When ECH is added at low density, typically for $\overline{n}_e < 4.5 \cdot 10^{19} m^{-3}$, T_i drops by up to 30%, while T_e remains essentially unchanged. During the EC-heated phase T_e/T_i approaches unity and the dependence of T_e and T_i on $\overline{n}_e$ becomes very similar. The effect of adding electron heating is better seen in figure 3, which shows the behaviour of T_e/T_i with respect to the applied ECH power: with increasing electron heating, the electron to ion temperature ratio increases from $T_e/T_i \sim 0.7$ to $T_e/T_i \sim 1$, mostly because of the drop of T_i.

The gradients of the experimental profiles are essential to study and to understand transport. Figure 4 shows the behaviour of the normalised gradient lengths $R/L_{T_{e,i}} = R \cdot |\nabla T_{e,i}/T_{e,i}|$ with respect to T_e/T_i. All the gradients are calculated with respect to the minor radius defined for the linear gyro-kinetic code GS2 [15] (used later for comparison in the modelling section). In figure 4 (a), we observe that R/L_{T_i} decreases with increasing T_e/T_i. The highest R/L_{T_i} (points in figure with $R/L_{T_i} \geq 7$ and $0.7 \leq T_e/T_i \leq 0.8$) are obtained during NBI-only phases of the discharges. These points correspond to the highest T_i shown in figure 2 (a) and are reached only at low density. When

ECH is added, higher T_e/T_i and lower R/L_{T_i} are measured. The same plot for R/L_{T_e} is shown in figure 4 (b), which exhibits a weak correlation between R/L_{T_e} and T_e/T_i. Considering figures 2, 3 and 4, we can state that, when EC electron heating is added, the T_i profiles flatten, the T_e profiles almost do not change and T_e/T_i increases. Consequently, adding electron heating in these discharges has a negative effect on the global thermal confinement time, which decreases by up to 30% [14].

Another parameter also subject to variations when ECH is applied is the plasma toroidal velocity v_ϕ, and in particular its gradient ∇v_ϕ. As mentioned above, ∇v_ϕ is an important parameter because it influences the ion heat transport through its parallel component in $\nabla v_\parallel$, which has a destabilising effect on the ITG, and through the $\omega_{E\times B}$ term, which has a stabilising effect. Figure 5 shows the T_e/T_i dependence of $R \cdot \nabla v_\phi / v_{thi}$ (v_{thi} is the ion thermal velocity) for the discharges of figure 4. The dependence of $R \cdot \nabla v_\phi / v_{thi}$ on T_e/T_i is similar to that of R/L_{T_i}: ∇v_ϕ decreases with increasing T_e/T_i.

Figure 6 shows that there is also a strong correlation between R/L_{T_i} and $R \cdot \nabla v_\phi / v_{thi}$. A colour-code for T_e/T_i indicates the different range of excursion of R/L_{T_i}. A consequence of the link between heat and momentum transport [21, 22] and of the used sources of power and momentum is that ∇T_i and ∇v_ϕ are also strongly correlated. For the ions, in steady state, we can write the following relationships:

$$\chi_i \cdot |\nabla T_i| = \frac{1}{n} \int P_i \cdot dV, \tag{1}$$

$$\chi_\phi \cdot |\nabla v_\phi| = \frac{1}{n} \int S_\phi \cdot dV, \tag{2}$$

where χ_i and χ_ϕ are the heat and momentum diffusivities, P_i and S_ϕ the sources of ion power and momentum. Since all these experiments are performed with the same NBI injectors, at fixed power and without any other source of ion heat and momentum, the integral ratio is constant:

$$\frac{\chi_i \cdot \nabla T_i}{\chi_\phi \cdot \nabla v_\phi} = \frac{\int P_i \cdot dV}{\int S_\phi \cdot dV} = const. \tag{3}$$

Therefore, a strong correlation between ∇T_i and ∇v_ϕ is expected. In addition, it must also be underlined that a constant ratio between χ_i and χ_ϕ does not automatically lead to a strong correlation between R/L_{T_i} and ∇v_ϕ. In fact, if we assume the case of an ITG plasma with very strong stiffness, a constant ratio χ_i/χ_ϕ would lead to a constant ratio $\nabla T_i/\nabla v_\phi$, but, because of the profile stiffness, to a constant value of the R/L_{T_i} threshold. Since in the experiments we observe clear variations of R/L_{T_i}, this mechanism is not sufficient to explain these R/L_{T_i} variations and the existence of another mechanism must be assumed: $E \times B$ shearing stabilisation is likely to play this role, as it will be shown later. For the particular discharges presented in this paper, figure 6 points out the following: (i) peaked ion temperatures (high R/L_{T_i}) are obtained in plasmas with low values of T_e/T_i (hot ions) and high ∇v_ϕ, conditions mostly fulfilled at lower densities; (ii) when ECH is added, T_e/T_i increases and ∇v_ϕ decreases, inducing a reduction of R/L_{T_i}; (iii) low R/L_{T_i} are coupled to low ∇v_ϕ and high T_e/T_i.

The causality is suggested by the time evolution of the plasma energy when ECH is applied [14]. Even when adding the maximum available $2MW$ of ECH, the stored energy remains basically unaffected, except for a very short transient time in the very beginning, within approximately $150ms$ after the ECH switch on. During this time, a small raise on the time scale of the T_e increase is measured, but it is shortly followed by a subsequent decrease correlated to the falls of T_i and v_ϕ. A possible explanation could be that the initial increase of T_e destabilises the ITG leading to an increase in ion transport [19], therefore to a reduction of both T_i and R/L_{T_i}. Since ion heat and momentum transport are coupled [21, 22, 23], momentum transport would also increase, leading to a decrease of ∇v_ϕ and of the $\omega_{E\times B}$ stabilisation. The two effects would therefore both contribute to the reduction of R/L_{T_i}. In the next section we will make use of theory based transport models to put in evidence the combined effects of T_e/T_i and ∇v_ϕ.

3 Modelling and comparison with experiments

In order to try and separate the role of T_e/T_i and ∇v_ϕ, and possibly also to quantify each contribution, modelling using the gyro-Landau-fluid transport model GLF23 [25] and the linear gyrokinetic code GS2 [15] has been performed. Both models allow the determination of the growth rate γ of the most unstable mode, in our case the ITG. The GS2 calculations of γ are much more precise than those yielded by GLF23. GLF23, implemented in the ASTRA transport code [27], allows a consistent simulation of the main plasma profiles and yields the contribution of ∇v_ϕ through the

calculation of the $E \times B$ shearing rate using the formula $\omega_{E\times B} = (r/q)d(E_r/B_pR)/dr$ [26]. We combine the results of the two codes to calculate the effective ITG growth rates $\gamma_{eff} = \gamma - \omega_{E\times B}$, which accounts for rotational shear stabilisation. Therefore, combining GS2 with GLF23 allows to join precise calculations of the growth rate and of its linear threshold using GS2, with consistent GLF23 calculations of $\omega_{E\times B}$ using the experimental profiles.

In our study, we use as reference case a low density discharge ($T_e/T_i(\rho_t = 0.5) = 0.7$, NBI-only phase at $P_{NBI} = 5.0MW$) to investigate the influence of ∇v_ϕ on R/L_{T_i} with GLF23. The main results of a full simulation of this reference case discharge are reported in appendix A. It is in particular shown that GLF23 correctly reproduces the changes in the temperature and density profiles induced by the application of the ECH. In appendix A we also show how we used different values of ∇v_ϕ to investigate the role of this parameter. The temperature ratio at $\rho_t = 0.5$ is almost unaffected by the ∇v_ϕ scan and stays at $T_e/T_i \sim 0.7$. Figure 7 shows the results of these GLF23 simulations at $\rho_t = 0.5$. Figure 7 (a) illustrates the dependence of the ITG growth rate γ, of the $\omega_{E\times B}$ stabilisation term and of the effective growth rate $\gamma_{eff} = \gamma - \omega_{E\times B}$ on ∇v_ϕ. The dependence of γ and of $\omega_{E\times B}$ on ∇v_ϕ shows the same trend and quite comparable variations. Although γ increases, because of the slightly stronger increase of $\omega_{E\times B}$, the effective growth rate γ_{eff} decreases, allowing a higher ion temperature peaking to be reached, as shown in figure 7 (b). In order to drive the flux imposed by the NBI heating, the model "adjusts" the temperature gradients, shown in figure 7 (b). On the other hand, the variations induced on the electron temperature peaking are weak. Hence, at constant density, increasing ∇v_ϕ induces only an increase in R/L_{T_i}, due to the decrease of γ_{eff}, while T_e/T_i is unchanged. Other scans were performed at different values of T_e/T_i as well.

In order to analyse independently the T_e/T_i dependence of transport, the GS2 code has been used. The GS2 calculations of the dependencies of the ITG growth rate with respect to T_e/T_i and R/L_{T_i} have been performed with parameters taken at mid radius ($\rho_t = 0.5$), in particular with $R/L_n = 4.0$ and $R/L_{T_e} = 5.0$. Figure 8 shows the following: (i) at constant T_e/T_i, as expected, the mode has a threshold in R/L_{T_i} above which the growth rate γ increases; (ii) the threshold depends on T_e/T_i: increasing T_e/T_i destabilises the ITG via the decrease of the threshold; (iii) at constant R/L_{T_i}, increasing T_e/T_i induces an increase of the growth rate. Linear GS2 calculations do not allow to take into account consistently the effect of a rotational $E \times B$ shear on the growth rate. In order to include this effect in the GS2 growth rates, the $\omega_{E\times B}$ yielded by GLF23 for corresponding cases are used to calculate the effective GS2 growth rate γ_{eff}. In figure 8, parallel dashed line indicate the $\omega_{E\times B}$ values corresponding to three values of ∇v_ϕ. The effective threshold, $R/L_{T_i}^{eff}$, is determined by the intersections of the curves $\gamma(T_e/T_i)$ and $\omega_{E\times B}(v_\phi)$. Hence, for a given heat flux, the $\omega_{E\times B}$ stabilisation increases the effective threshold allowing to reach higher values of R/L_{T_i}. For example, in the reference case the effective threshold is increased from $R/L_{T_i}^{eff} \sim 4$ to $R/L_{T_i}^{eff} \sim 7$.

Figure 9 shows the comparison between experimental measurements of R/L_{T_i} and modelling predictions for the dependence of $R/L_{T_i}^{eff}$ on T_e/T_i. The experimental R/L_{T_i} dependence on T_e/T_i is compared with the linear GS2 thresholds for the cases with and without the correction by $\omega_{E\times B}$. We can state the following: (i) in both cases, the experimental points lay above the two threshold curves, as expected; (ii) $\omega_{E\times B}$ brings the threshold closer to the measured R/L_{T_i}, which is consistent with high T_i stiffness. In addition, taking $\omega_{E\times B}$ into account provides a better apparent T_e/T_i dependence compared to the experimental data.

These effects are investigated in more detail in figure 10, where the experimental R/L_{T_i} dependence on ∇v_ϕ is compared with the modelling predictions of GS2 and GLF23. The colour code for the experimental points indicates the T_e/T_i ranges. For GS2, the points shown in the figure correspond to the effective thresholds $R/L_{T_i}^{eff}$ for different values of T_e/T_i. For GLF23, the line at $T_e/T_i = 0.7$ has been deduced from the simulations described for figure 7. Similar ∇v_ϕ scans performed for $T_e/T_i = 1.0$ and 1.2 are also reported. We observe the following: (i) both models predict the increase of R/L_{T_i} with ∇v_ϕ, but their slopes are lower on average by a factor of 2; (ii) considering the GS2 linear thresholds, if the experimental T_e/T_i variations are also taken into account, then the slope from the modelling (dashed line) is much closer to the experimental one; (iii) all GLF23 curves lay above the ones for GS2 for the corresponding T_e/T_i value, which is consistent with the fact that GLF23 provides the R/L_{T_i} of the full simulation, while GS2 provides the effective thresholds $R/L_{T_i}^{eff}$.

Summarising, from figure 9 we see that the changes in T_e/T_i alone are not sufficient to explain the measured variations in R/L_{T_i}, just as from figure 10 we see that the changes in ∇v_ϕ alone are also not sufficient. The combined effects of both parameters are needed in order to cover the experimental R/L_{T_i} variations. Therefore, the combined effects of the increase of T_e/T_i and of the decrease of ∇v_ϕ contribute to the decrease of R/L_{T_i} and to the confinement degradation. Since the parameters changes are induced by the switching on of the ECH, the loop leading to the degradation is most likely started by the first increase of T_e/T_i due to the increase in T_e; as a consequence, the increased

T_e/T_i induces a decrease of the ITG threshold and therefore an increased ion heat transport; because of the link between ion heat and momentum transport, the latter will also be enhanced, leading to a decrease of ∇v_ϕ; the decrease of ∇v_ϕ will produce a decrease of the $E \times B$ shearing stabilisation, hence to a more pronounced decrease of the ITG effective threshold. This loop stops once the profiles reach the gradients needed in order to sustain the externally imposed heat flux, i.e. just above the threshold.

4 Conclusions

In this paper, the effects of ECH electron heating on the ion heat transport in NBI-heated H-mode plasmas have been studied. In particular, the correlation between ion heat transport, related to R/L_{T_i}, on T_e/T_i and ∇v_ϕ has been investigated and compared with calculations made with the GLF23 and GS2 codes.

Experimentally it is observed that, at constant NBI power, T_e/T_i decreases with decreasing density (up to $T_e/T_i \sim 0.6$). Simultaneously, high values of ∇v_ϕ and of R/L_{T_i} are also reached, leading to good confinement properties. When pure electron heating is added with ECH, T_e/T_i increases (mostly because of the decrease of T_i), ∇v_ϕ decreases and the heat transport in the ion channel is enhanced, leading to a decrease of R/L_{T_i}. These effects are particularly evident at low densities. R/L_{T_i} and ∇v_ϕ are both correlated to T_e/T_i, while R/L_{T_i} is also strongly correlated to ∇v_ϕ itself. High R/L_{T_i} are reached only for low values of T_e/T_i and high values of ∇v_ϕ and vice-versa.

Modelling with GS2 and GLF23 shows that ∇v_ϕ is stabilising the ITG mode through the $\omega_{E\times B}$ shearing rate (see also [23]): increasing ∇v_ϕ allows to reach higher values of R/L_{T_i}. GS2 calculations show that, with increasing T_e/T_i, the ITG threshold in R/L_{T_i} decreases, inducing an increase of the growth rate at given R/L_{T_i}. The $E \times B$ shearing rate, which depends on ∇v_ϕ, stabilises the ITG through the decrease of the effective threshold via $\gamma_{eff} = \gamma - \omega_{E\times B}$. The comparison of the experimental data with the modelling calculations shows that the single effect of T_e/T_i or ∇v_ϕ only is not sufficient to explain the changes measured in R/L_{T_i}, with the difference being of the order of 2. The full variations in R/L_{T_i} are only obtained if the combined changes of T_e/T_i and ∇v_ϕ are considered.

The confinement degradation is a consequence of the addition of ECH electron heating. Therefore, the loop which leads to the degradation is likely to be started by a first increase of T_e/T_i due to an increase in T_e; the increased T_e/T_i provokes a decrease of the ITG threshold and an increase of ion heat transport and, because of the strong link, of momentum transport, which leads to a decrease of ∇v_ϕ; the decrease of ∇v_ϕ produces a decrease of the $E \times B$ shearing stabilisation, hence a more pronounced decrease of the ITG effective threshold. This loop stops once the profiles reach the gradients needed in order to sustain the externally imposed heat flux, i.e. just above the threshold.

Figure 11 shows the results of the GLF23 simulations of the reference case mentioned in section 3. The modelled experiment is the ASDEX Upgrade, low density, H-mode discharge 17219 [14]. This experiment has been performed with plasma current $I_P = 1.0MA$, toroidal field $|B_T| = 2.4T$, elongation $\kappa = 1.7$, triangularity $\delta = 0.15$ and edge safety factor $q_{95} \sim 4.5$. The model has been used to simulate two distinct phases: a first one in which only NBI heats the plasma ($P_{NBI} = 5.0MW$, empty symbols and dashed lines) and a second one in which $2.0MW$ of ECH are added at $\rho_t = 0.25$ (full symbols and full lines). The boundary condition has been set at $\rho_t = 85$. From the figures it is seen that all the profiles, T_e, T_i and n_e, are reasonably well reproduced. Although T_i is slightly over-estimated and T_e slightly under-estimated, the model reproduces the behaviour of the profiles when the ECH is applied: T_i decreases strongly, T_e increases slightly, the central electron density is slightly reduced and T_e/T_i increases.

Figure 12 shows the v_ϕ profiles imposed within GLF23 to investigate the effects on transport of varying ∇v_ϕ. The different values of ∇v_ϕ have been obtained by imposing different v_ϕ profiles: its value at the centre has been changed, while the edge value was kept constant. In order to avoid transport changes induced by density variations, in these simulations the density profile was kept fixed. In the transport equations of the model, only the gradient of the toroidal velocity plays a role for the determination of the $\omega_{E\times B}$ term [25], hence imposing different absolute values does not influence the simulations.

Acknowledgements

We are very grateful to R. E. Waltz and J. E. Kinsey for having provided us with GLF23 and to M. Kotschenreuther and W. Dorland for having provided us with GS2.

References

[1] Ryter F. et al, Plasma Phys. Control. Fusion **43** (2001) A323

[2] Ryter F. et al, Phys. Rev. Lett. **86** (2001) 2325

[3] Ryter F. et al, Phys. Rev. Lett. **86** (2001) 5498

[4] Hoang G. T. et al, Phys. Rev. Lett. **87** (2001) 125001

[5] Suttrop W. et al, Proc. 28th EPS Conf. on Controlled Fusion and Plasma Physics, (Madeira 2001), vol 25A (*Europhysics Conference Abstracts*) ed R. Pick (Geneva:EPS) 989, CD-ROM

[6] Jacchia A. et al, Nuclear Fusion **42** (2002) 1116

[7] DeBoo J. et al, Nuclear Fusion **45** (2005) 494

[8] Camenen Y. et al, Plasma Phys. Control. Fusion **47** (2005) 1971

[9] Burrell K. H. et al, in Plasma Physics and Controlled Nuclear Fusion Research, Washington, DC, 1990 (IAEA, Vienna, 1991), Vol. 1, p. 123

[10] Thompson E. et al, Phys. Fluids B **5** (1993) 246

[11] Strachan J. D. et al, Phys. Rev. Lett. **58** (1987) 1004

[12] Sips A. C. C. et al, Plasma Phys. Control. Fusion **44** (2002) B69

[13] Wolf R. C. et al, Plasma Phys. Control. Fusion **45** (2003) 1757

[14] Manini A. et al, Plasma Phys. Control. Fusion **46** (2004) 1723

[15] Kotschenreuther, M. et al, Com. Phys. Communication **88** (1995) 128

[16] Petty C. C. et al, Phys. Rev. Lett. **83** (1999) 3661

[17] De Boo J. C. et al, Nuclear Fusion **39** (1999) 1935

[18] Mantica P. et al, O3.1A, 30th EPS Conference on Controlled Fusion and Plasma Physics (2003), St. Petersburg, Russia

[19] Weiland J. et al, Plasma Phys. Control. Fusion **47** (2005) 441

[20] Asp E. et al, Plasma Phys. Control. Fusion **47** (2005) 505

[21] Kallenbach A. et al, Plasma Phys. Control. Fusion **33** (1991) 595

[22] Nishijima D. et al, Plasma Phys. Control. Fusion **47** (2005) 89

[23] Peeters A. G. et al, Phys. Palsmas **12** (2005) 072515

[24] Petty C. C. et al, Phys. Plasmas **9** (2002) 128

[25] Waltz R. E. et al, Phys. Plasmas **7** (1997) 2482

[26] Waltz R. E. et al, Phys. Plasmas **6** (1999) 4265

[27] Pereverzev G. and Yushmanov, P. N., IPP Internal Report, IPP 5/98 (2002)

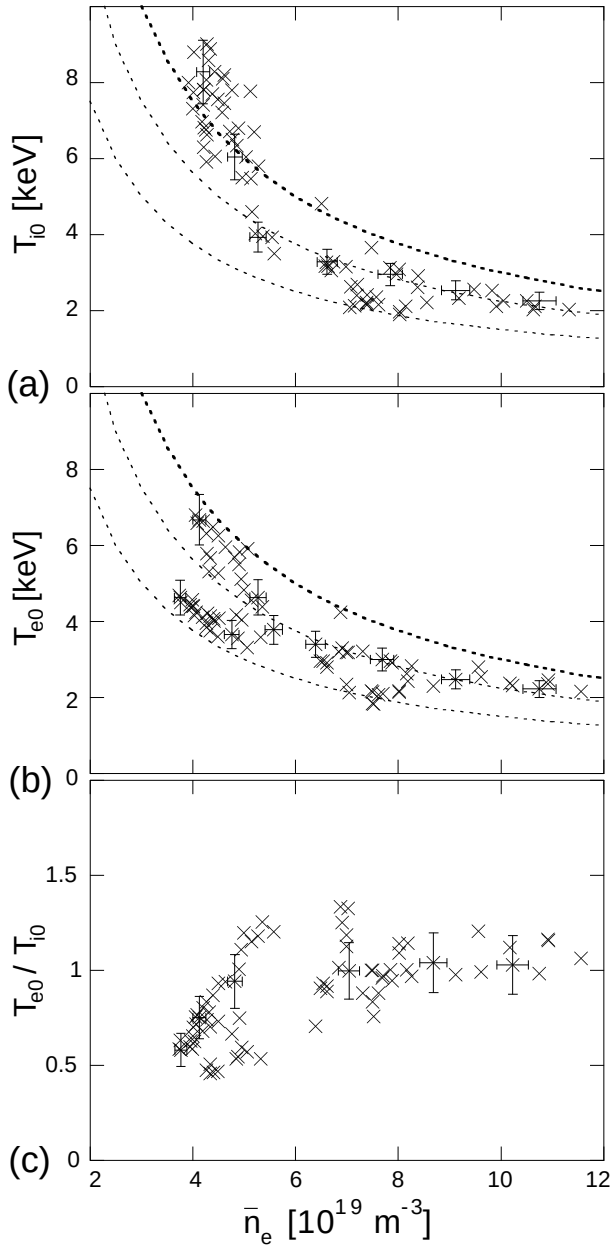

Figure 1: Behaviour of central (a) ion, T_{i0}, and (b) electron, T_{e0}, temperature with respect to averaged line integrated electron density, $\overline{n}_e$, for H-mode plasmas heated by NBI only. (c) Behaviour of the ratio T_{e0}/T_{i0} with respect to $\overline{n}_e$. between Strong variations are observed especially for $n_e < 6.0 \cdot 10^{19} m^{-3}$. The dotted lines in (a) and (b) indicate the lines of constant pressure $p \sim n \cdot T$.

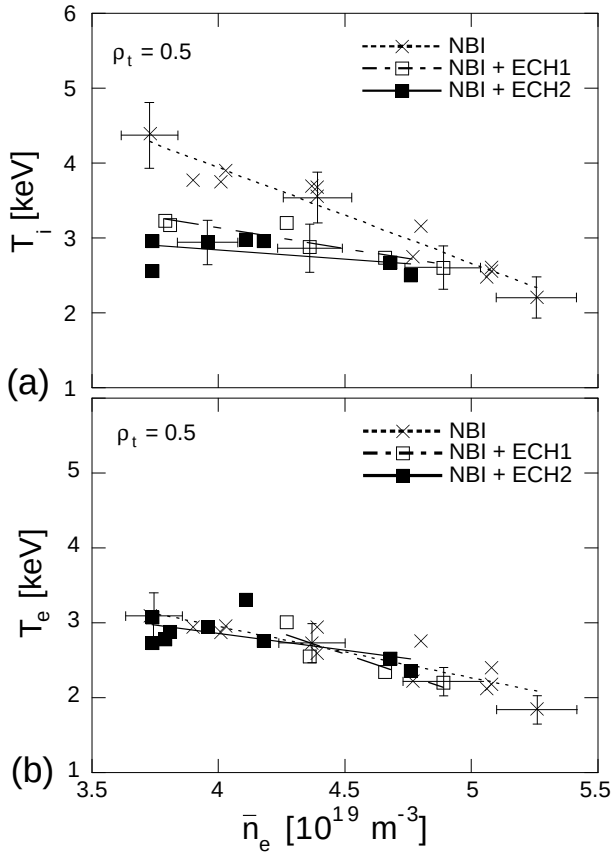

Figure 2: Behaviour of (a) ion and (b) electron temperature at $\rho_t = 0.5$ with respect to line integrated electron density. Comparison between NBI-only (crosses) and NBI plus low power ECH ($P_{ECH} < 1MW$, empty symbols, ECH1) and NBI plus high power ECH ($P_{ECH} > 1MW$, full symbols, ECH2). The lines are linear fits through the experimental data points.

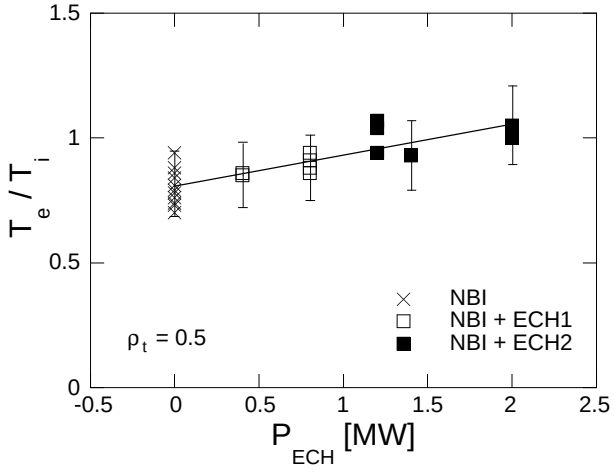

Figure 3: Dependence of T_e/T_i on the applied ECH power. The lines are linear fits through the experimental data points.

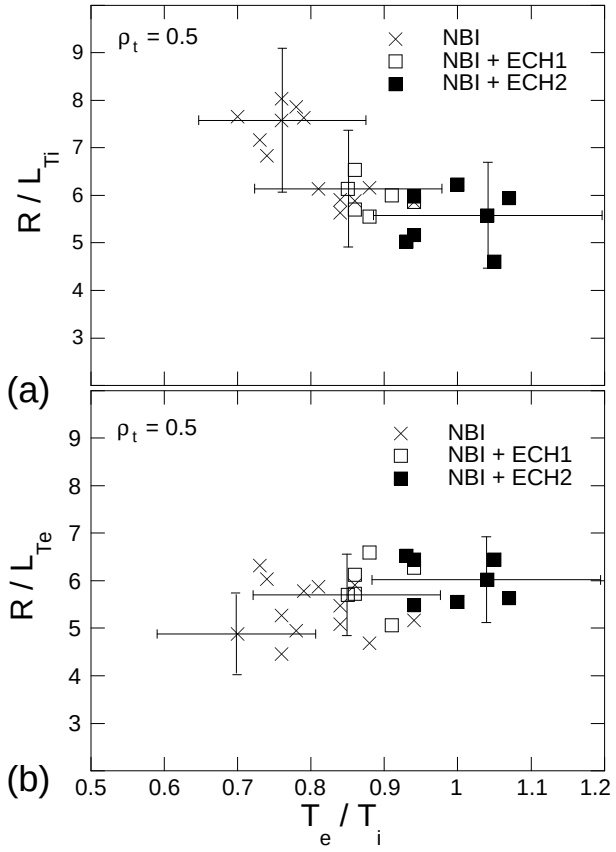

Figure 4: Behaviour of normalised gradient length of (a) ion and (b) electron temperature with respect to temperature ratio T_e/T_i and for different ECH power levels.

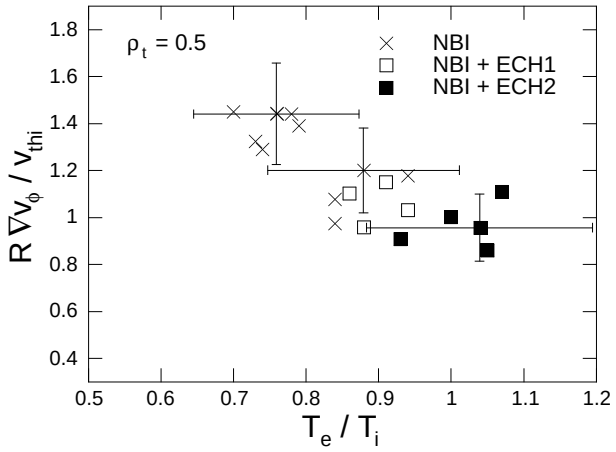

Figure 5: Behaviour of $R \cdot \nabla v_\phi / v_{thi}$ with respect to T_e/T_i and for different ECH power levels.

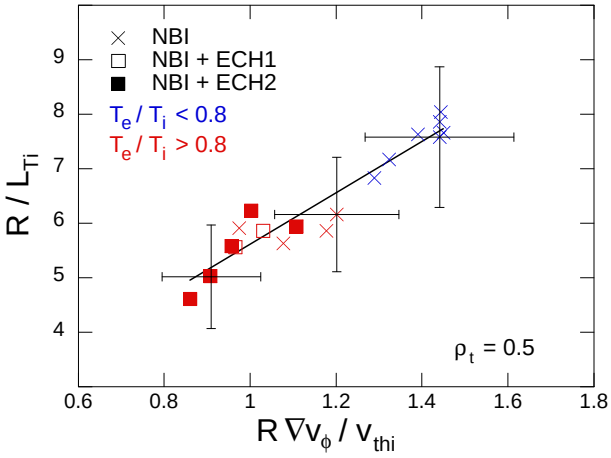

Figure 6: Dependence of R/L_{T_i} on $R \cdot \nabla v_\phi / v_{thi}$ and T_e/T_i. The line is a linear fit through the data points.

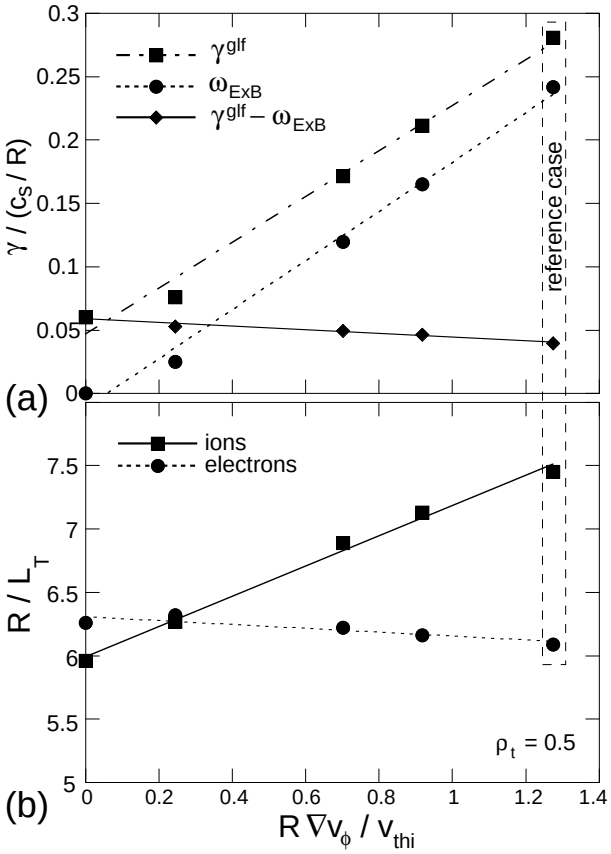

Figure 7: Modelling using GLF23. (a) Dependence of the ITG growth rate γ, of the $\omega_{E\times B}$ stabilisation term and of the effective growth rate $\gamma_{eff} = \gamma - \omega_{E\times B}$ on ∇v_ϕ. (b) Dependence of $R/L_{T_{e,i}}$ on ∇v_ϕ.

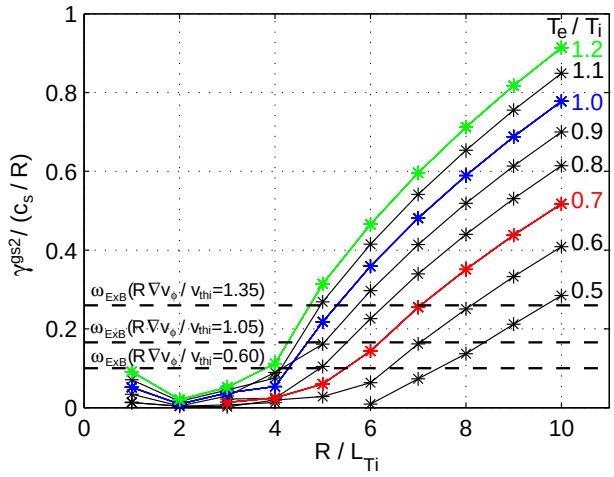

Figure 8: GS2 scan of the growth rate γ scanned w.r.t. R/LT_i and T_e/T_i with $R/L_n = 4.0$ and $R/L_{T_e} = 5.0$. The $\omega_{E\times B}$ corresponding to three values of $R \cdot \nabla v_\phi / v_{thi}$ are also shown.

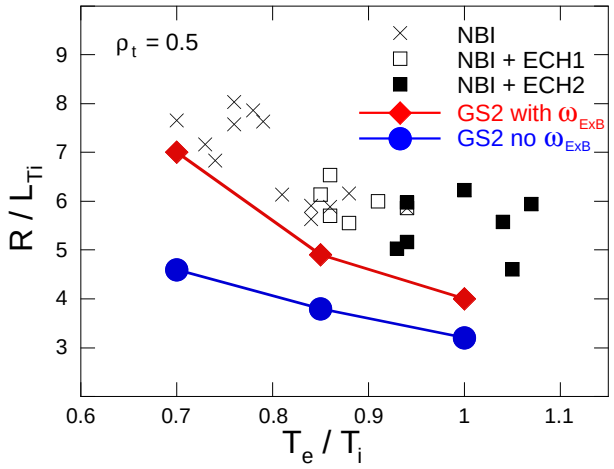

Figure 9: R/L_{T_i} dependence on T_e/T_i: comparison with $(R/L_{T_i})_{crit}$ from GS2 with and without considering $\omega_{E\times B}$.

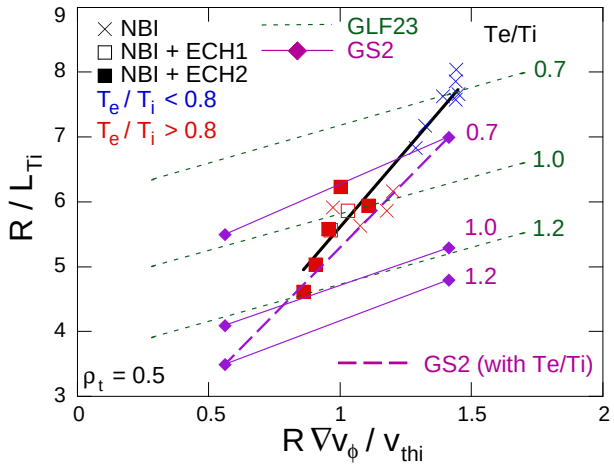

Figure 10: R/L_{T_i} dependence on $R \cdot \nabla v_\phi / v_{thi}$: comparison with GS2 and GLF23.

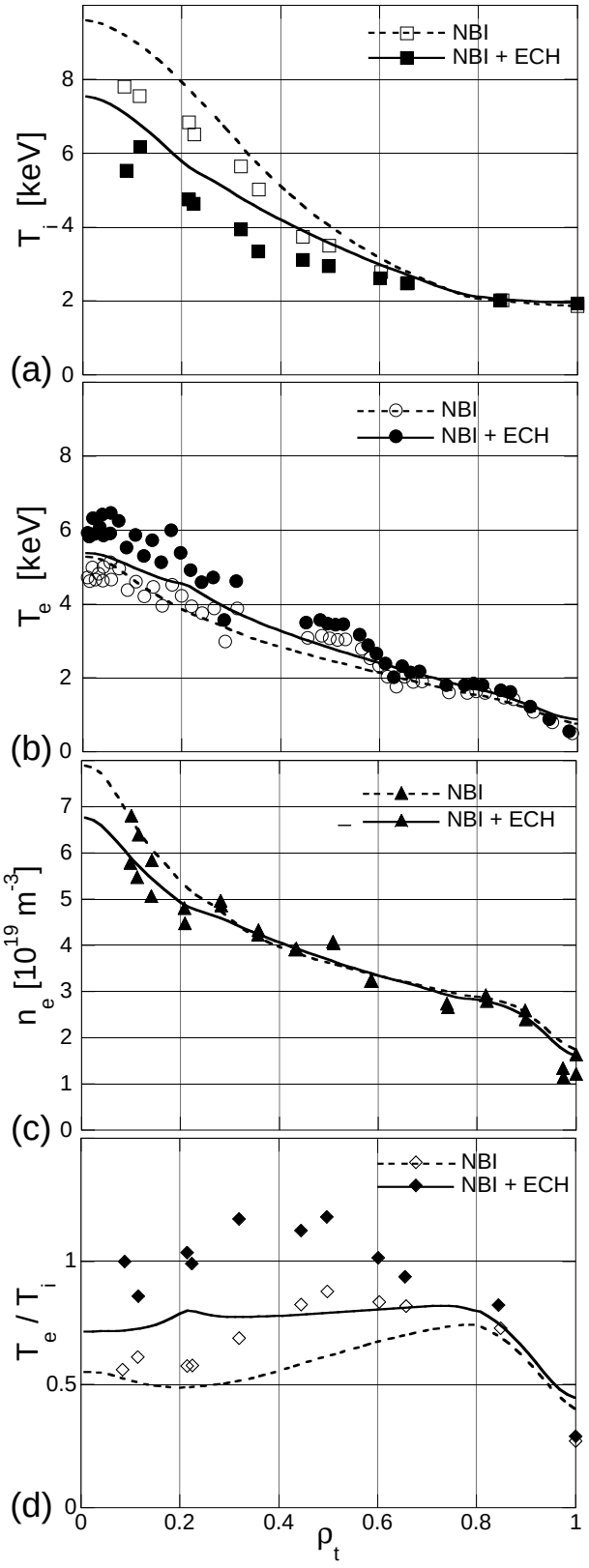

Figure 11: Results of GLF23 simulation of the reference discharge. (a) Ion temperature; (b) electron temperature; (c) electron density (measured with the Thomson scattering diagnostic); (d) T_e/T_i.

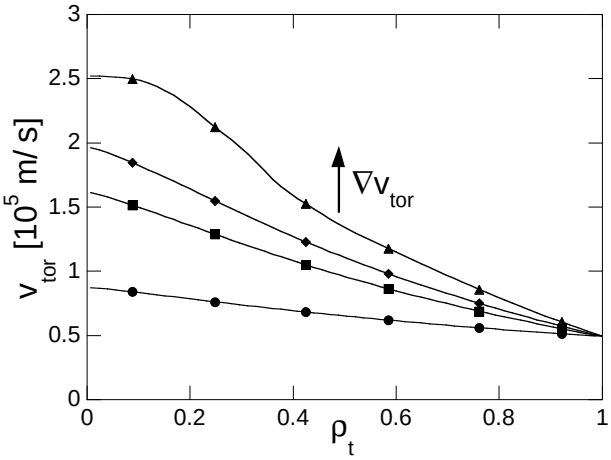

Figure 12: Profiles of v_ϕ imposed to scan the ∇v_ϕ influence on T_e and T_i.